communications earth & environment

Article

https://doi.org/10.1038/s43247-024-01529-x

A unique warm–water oasis in the Siberian Arctic's Chaun Bay sustained by hydrothermal groundwater discharge

Alexander N. Charkin[1] ✉, Ksenia N. Kosobokova[2], Elizaveta A. Ershova[3], Vitaly L. Syomin[2], Glafira D. Kolbasova[2,4], Pavel Yu. Semkin[1], Andrey E. Leusov[1], Oleg V. Dudarev[1], Timofey A. Gulenko[1], Elena I. Yaroshchuk[1], Anatoly M. Startsev[1], Pavel A. Fayman[1], Vladislav A. Krasikov[1], Sergey A. Zverev[1], Elena A. Bessonova[1], Alexander S. Ulyantsev[2], Evgeny V. Elovsky[5], Daria A. Yurikova[2], Kirill A. Kobyakov[6], Olga L. Zimina[7], Alexandra V. Gerasimova[8], Peter P. Tishchenko[1] & Alexander A. Didov[1]

Chaun Bay, located on the fringe of the East Siberian Sea, has been described since the mid-20th century to support a unique marine ecosystem that is atypical for the local Siberian Arctic. Here we use ship-board physical, biogeochemical and geological measurements taken in October 2020, along with hydrographic observations taken from land-fast ice in April 2023, to demonstrate that these warm-water biological communities are supported by hydrothermal submarine groundwater discharge that delivers heat, salinity, nutrients, and trace elements to the bay. We identify a cyclonic eddy that mixes the warm nutrient-rich groundwater with oxygen-rich surface water, resulting in a water mass within Chaun Bay that has similar physical and chemical properties to the highly productive waters of the North Pacific and Southern Chukchi Sea. The bay showed elevated concentrations of chlorophyll-a and zooplankton, and the abundance and species diversity of epibenthos significantly exceeded values observed elsewhere in the East Siberian Sea. The benthic communities contained a number of boreal species that are not typically found in the Arctic Ocean. We also observed *Thysanoessa* krill populations, a pelagic species generally considered an expatriate in Arctic waters.

Chaunskaya Bay, or Chaun Bay, located in the East Siberian Sea (ESS), harbors unique benthic communities whose peculiarities have been noted since the mid-20th century[1]. In the late 1980s, the ecosystem of the bay was described in detail by an expedition of the USSR Academy of Sciences' Zoological Institute[2]. This expedition discovered a number of boreal species previously unrecorded anywhere else in the Siberian Arctic (Fig. 1). They also found that the currents dominating in the bay had a markedly cyclonic structure due to the northern incoming waters of the Kolyma River and other smaller rivers with poor primary production, while primary production within the bay itself was fairly high. Water temperatures reached 12 °C in summer near both the water surface and the bottom. The researchers also identified an unusual water layer, which in its physical and chemical properties[3], as well as planktonic communities, resembled the boreal–arctic Pacific water mass[2]. It was hypothesized that the boreal species not typical of the Siberian Arctic could have found their way to this region during the last climatic optimum[4], yet their survival mechanisms in this partially isolated and climatically harsh body of water remained a mystery.

Results and Discussion

To address this question, an expedition onboard the research vessel Akademik Oparin was carried out in October 2020 to Chaun Bay. This expedition collected a series of physical, biogeochemical, and geological measurements, as well as samples of planktonic and benthic communities (Fig. 1; Supplementary Figs. 1, 2). Additionally, in April 2023, hydrological observations were carried out from land-fast ice located in the straits

[1]Pacific Oceanological Institute, Russian Academy of Sciences, 43, Baltiyskaya Street, Vladivostok 690041, Russia. [2]Shirshov Institute of Oceanology, Russian Academy of Sciences, 36, Nahimovskiy prospekt, 117997 Moscow, Russia. [3]Institute of Marine Research (IMR), Bergen, Norway. [4]N.A. Pertsov White Sea Biological Station, Lomonosov Moscow State University, Leninskie Gory, 1, building 12, 119234 Moscow, Russia. [5]Far East Geological Institute, Russian Academy of Sciences, 159, Prospekt Stoletiya, Vladivostok 690022, Russia. [6]Kaliningrad State Technical University, Sovetskiy av., 1, 236022 Kaliningrad, Russian Federation. [7]Murmansk Marine Biological Institute of Russian Academy of Sciences, Vladimirskaya str., 17, 183010 Murmansk, Russia. [8]St. Petersburg State University, 16th Line VO, 29, 199178 St. Petersburg, Russia. ✉e-mail: charkin@poi.dvo.ru

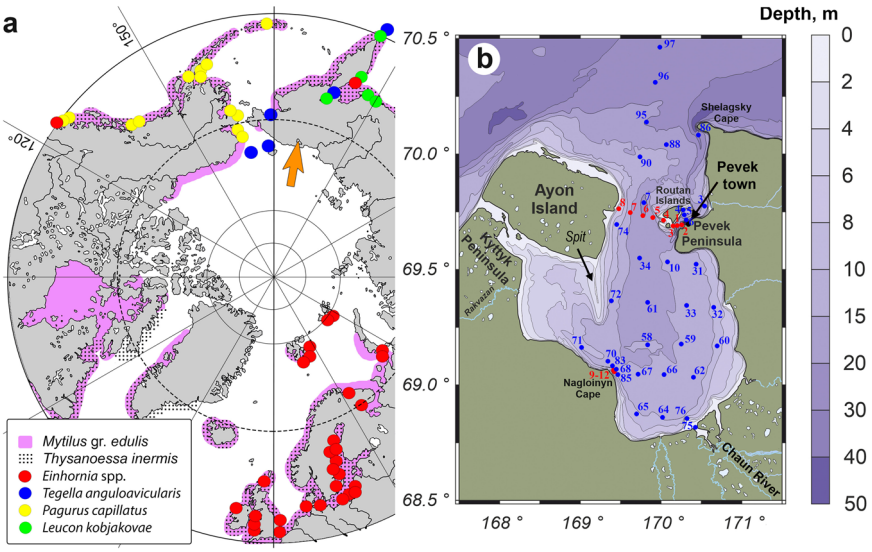

Fig. 1 | An overview map of the Arctic Ocean and position of the Chaun Bay. a Chaun Bay location in the Arctic (orange arrow). The different symbols show the documented world-wide distribution of benthic and planktonic species found in Chaun Bay[2,33–37,63–67]. **b** Station locations, as well as the bathymetry and main geographical features of Chaun Bay. Blue represents stations collected in October 2020, while red indicates stations sampled in April 2023.

between Chaun Bay and the ESS, as well as off Cape Naglyoynyn within Chaun Bay (Fig. 1).

In 2020, the study was carried out at the very end of climatic autumn (late October), just prior to ice freeze-up, when air temperatures ranged between −4.5 and +2 °C and surface water temperatures were as low as 0 °C in the western part of the bay. We discovered several distinct seafloor temperature anomalies where the temperature fell within the range between +2 and +3.5 °C (Supplementary Table 1; Fig. 2a; Supplementary Figs. 5–9), in sharp contrast with surrounding waters. The temperature anomaly near Cape Naglyoynyn had an obvious shape of a fluid plume in the vertical profile (Supplementary Figs. 6) and coincided with the salinity maximum (Supplementary Table 1; Fig. 2b; Supplementary Figs. 5, 6). Another salinity peak was identified south of the Pevek Peninsula; however, unlike the anomalies near Cape Naglyoynyn, the waters south of the Pevek Peninsula were characterized by lower temperatures (Supplementary Table 1; Fig. 2b; Supplementary Figs. 5–9). It is noteworthy that no waters with such high salinity (> 30 psu) were observed anywhere else in Chaun Bay or in the adjacent waters of the ESS down to 37 meters (Station 101), even more than 60 nautical miles from the entrance of the bay. The thermohaline anomalies occurred at depths of 10–15 meters near Cape Naglyoynyn and 15–20 meters near the Pevek Peninsula (Supplementary Table 1; Supplementary Fig. 5), and it is highly unlikely that these saline waters originated from the outer shelf of the ESS, at least during the period of our observations. There is no plausible explanation how such saline waters from the outer shelf could have ascended to a shallow water region and persisted there over extended periods in isolated spots, without any indication of their presence in either the bay's outer reaches or the neighboring East Siberian shelf. Furthermore, the positive temperatures of these waters dismiss the possibility that they are 'winter' waters. These findings clearly support an autochthonic origin, unrelated to winter processes.

The thermohaline anomaly near Cape Naglyoynyn was also observed under the ice in winter conditions, repeating the patterns observed in autumn, with the area showing the highest salinity and temperature relative to the waters in the straits between Chaun Bay and the ESS (Figs. 1, 3). In these straits the waters were well mixed in both shallow (13 meters) and deep (24 meters) layers, while the waters off Cape Naglyoynyn were well stratified, replicating the results observed during the autumn of 2020 at a depth of 14 meters (Station 68, or 11 in winter) (Fig. 3). The temperature-salinity plots showed two distinctly different patterns in the straits vs. near Cape Naglyoynyn (Supplementary Fig. 10). In the straits, we observed the predictable process of winter water cooling, convective mixing, and brine rejection under ice[5], resulting in the inverse relationship of temperature vs. salinity. In contrast, the source of heat near Cape Naglyoynyn were saline waters of unknown origin (Fig. 3; Supplementary Fig. 10). Furthermore, the ice thickness near Cape Naglyoynyn was 30 cm less than in the straits (120 cm vs. 150 cm) and the presence of numerous cracks in the ice around the cape prevented us from repeating the stations north of that area (summer Stations 70 and 71) due to safety concerns.

According to the Navigation Book[6] and other published data[2,7], the sea currents in Chaun Bay during the ice-free period are predominantly wind-driven and counter-clockwise. The continuous current in the strait between the Pevek Peninsula and Routan Islands flows northeast, and its velocity varies from 0.2 kn in summer to 0.1 kn in autumn, while tidal current velocities are within 0.2 kn[6]. The westerly and southerly winds that prevailed during our autumn studies also supported the cyclonic circulation (Supplementary Fig. 11). This long-term cyclonic circulation pattern is also supported by the presence of a narrow bar that extends more than 50 km southeast of Ayon Island, and was formed by the erosion of its coast by a southward-flowing current (Fig. 1).

The waters within the thermohaline anomalies near Cape Naglyoynyn during the autumn of 2020 were highly enriched in naturally occurring radium isotopes (Supplementary Table 2; Fig. 2; Supplementary Figs. 12, 13), which serve as prime indicators of submarine groundwater discharge (SGD)[8–11]. Specifically, activities of short-lived radium isotopes ranged from 20.6 to 31.7 dpm 100 L^{-1} for $_{ex}{}^{224}Ra$, 1.1 to 2.5 dpm 100 L^{-1} for $_{ex}{}^{223}Ra$ and 24 to 67 dpm 100 L^{-1} for ^{228}Ra near the Cape Naglyoynyn, in contrast to the bay's average values of 10.2, 0.6 and 47 dpm 100 L^{-1}, respectively. This strongly supports the notion that these high salinity waters, unique to this area and a closed anomaly south of the Pevek Peninsula, are of groundwater origin, dispersing in a cyclonic pattern to the east and north of Cape Naglyoynyn (Supplementary Tables 1, 2; Fig. 2; Supplementary Figs. 5, 7, 9). This conclusion is further supported by the activity ratio of $^{224}Ra/^{228}Ra$ and the concept of 'radium age'. The $^{224}Ra/^{228}Ra$ activity ratio was close to 1 at the anomaly sites in Cape Naglyoynyn area, which falls within the normal range in aquifers balanced by rock (1–2.2)[12]. Moving farther east and north of Cape Naglyoynyn, this ratio dropped to 0.1, a decline attributed to the differences in the radio isotopes' alpha decay rate (Supplementary Table 2; Fig. 2b; Supplementary Fig. 13). Modelling of the 'radium age', or the time elapsed since radium isotopes entered the water, indicated a rapid decay of 0.3–0.5 days in the presumed SGD locations near Cape Naglyoynyn but increased to 7.2–10.2 days in the northwestern part of the bay (Supplementary Table 2; Fig. 2c; Supplementary Fig. 12). This higher 'radium age' and the lower $^{224}Ra/^{228}Ra$ activity ratio in the near-bottom waters near the Pevek Peninsula suggest that this area is not a direct SGD location. However, the cyclonic structure of the currents and the high ^{228}Ra activity indicate that these waters also have a groundwater origin, and were likely transported there from SGD locations.

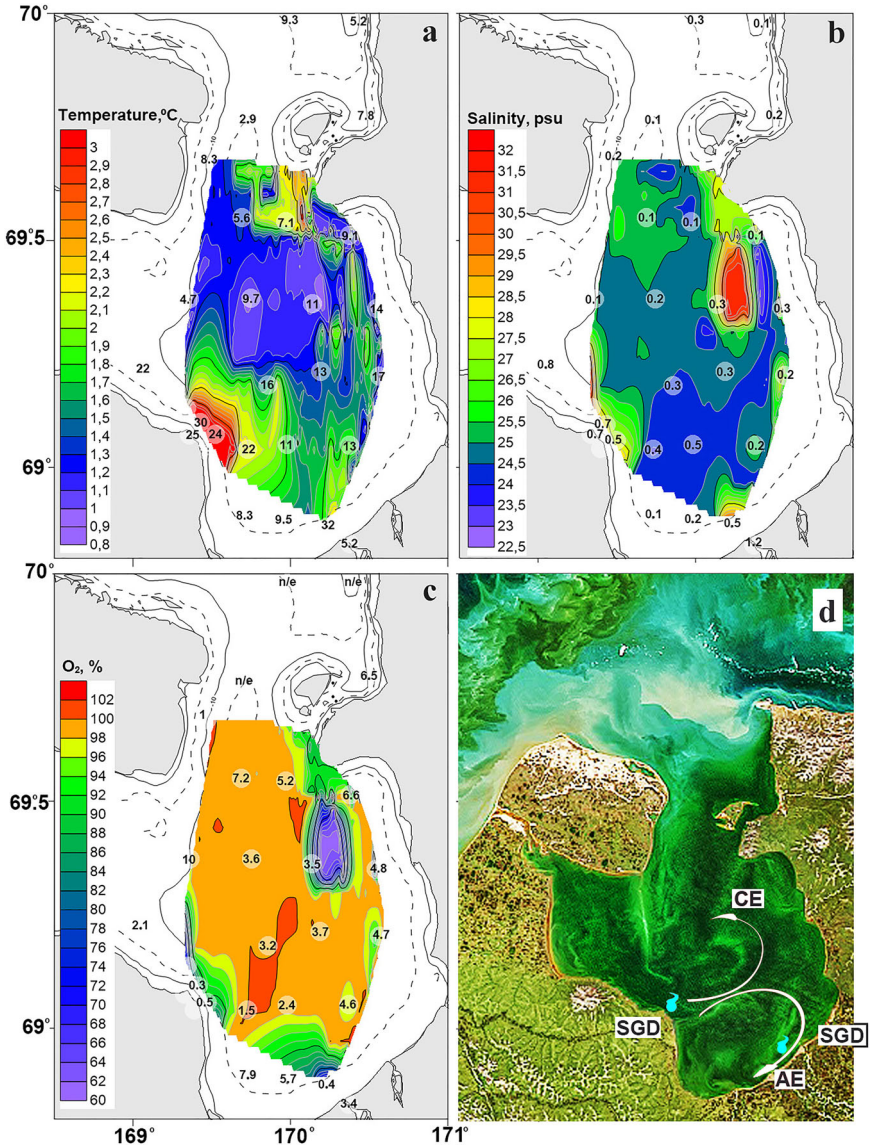

Fig. 2 | Spatial distribution of hydrological parameters at 8-meter depth, measured via the "Smart Fish" towed robotic system and satellite image of Chaun Bay. a Temperature. **b** Salinity. **c** Dissolved oxygen. **d** Satellite image of Chaun Bay in July 2020 (MODIS/Aqua image obtained on 20 July 2020 from https://worldview.earthdata.nasa.gov). The image shows cyclonic (CE) and anticyclonic (AE) eddies (marked with white arrows) also detected by our hydrological survey in October 2020. The blue dots show the cold/thermal submarine groundwater discharge location. Numbers in transparent circles indicate in the bottom horizon (**a**) activity of ex^{224}Ra (dpm 100 L^{-1}), (**b**) ^{224}Ra/^{228}Ra activity ratio, and (**c**) "radium age" (days).

Furthermore, data on naturally occurring radium isotopes (St. 76, 31.7 dpm 100 L^{-1} for $_{ex}$^{224}Ra, 1.3 dpm 100 L^{-1} for $_{ex}$^{223}Ra and 62 dpm 100 L^{-1} for ^{228}Ra) revealed a second SGD area near the mouth of the Chaun River in the southern part of the bay, charaterised by lower salinity due to its proximity of a fresh water source (Fig. 2, Supplementary Figs. 5, 7, 9, 12, 13). If station locations are sequentially connected from the youngest to the oldest radium ages in the near-bottom horizon, the result is a nearly closed cyclonic eddy pattern (Supplementary Fig. 14b) illustrating the bay's complex circulation across three directions (A–C, A–D and E–F) and revealing a fourth anticyclonic water flow in the southwestern part of the bay (A–B). By measuring the distance between the first and last points (Supplementary Fig. 14b), and knowing the time it took to travel this distance, we estimated the current velocities in these routes to be AB_v = 0.16 kn, AC_v = 0.43 kn, AD_v = 0.28 kn and EF_v = 0.26 kn. With the exception of the AC route, these velocities match the values obtained by direct measurements of currents in the bay (0.2 kn)[6], further supporting our conclusions. The surface flow dynamics were further complicated by wind activity. Surface waters showed a dispersal of the sequential radium age chains found near the seabed, with 'older' radium appearing in the western and central bay areas (Supplementary Fig. 14a). This distribution is attributed to the light, but persistent westerly winds that preceded our expedition and continued throughout its first half and drove waters from the bay's western shallow part towards the center (Fig. 1, Supplementary Fig. 11). Assuming a cyclonic circulation, this suggests that radium from the SGD area completes one eddy rotation before part of it is caught in a new eddy and the rest accumulates in the western shallow area due to the outer eddy's meandering (Fig. 1; Supplementary Fig. 14a). As a result, these short-lived isotopes which have not yet decayed are driven by westerly winds to the central part of the bay, significantly aging in the process. This is further supported by the high activity level of the long-lived isotope ^{228}Ra in the western part of the bay (Supplementary Fig. 13a). The half-life of radium ^{228}Ra is considerably longer (5.75 years) than ^{224}Ra and ^{223}Ra (3.66 and 11.4 days, respectively) which leads to its higher accumulation relative to the latter (Supplementary Fig. 13a).

As previously mentioned, while the second-high salinity area near the Pevek Peninsula is not an SGD location, is inherently linked to one. This anomaly was clearly bound by an oval shape, as visible on the temperature, salinity, and oxygen distribution plots produced by the Smart Fish towed robotic system (Fig. 2), and which was not related to the seabed topography (Fig. 1). Assuming a cyclonic circulation, it is likely that this anomaly represents the core of a cyclonic eddy, as supported both by our data and other observations[2,6,7], with the oval shape likely resulting from minor movements during Smart Fish profiling. However, any analysis of traditionally obtained oceanographic data will struggle to identify the presence of such a core, as it is highly dynamic. Shifts in wind direction during the latter half of our expedition could have moved this high-salinity core to the southwest, as seen in the CTD (Conductivity, Temperature, and Depth) -

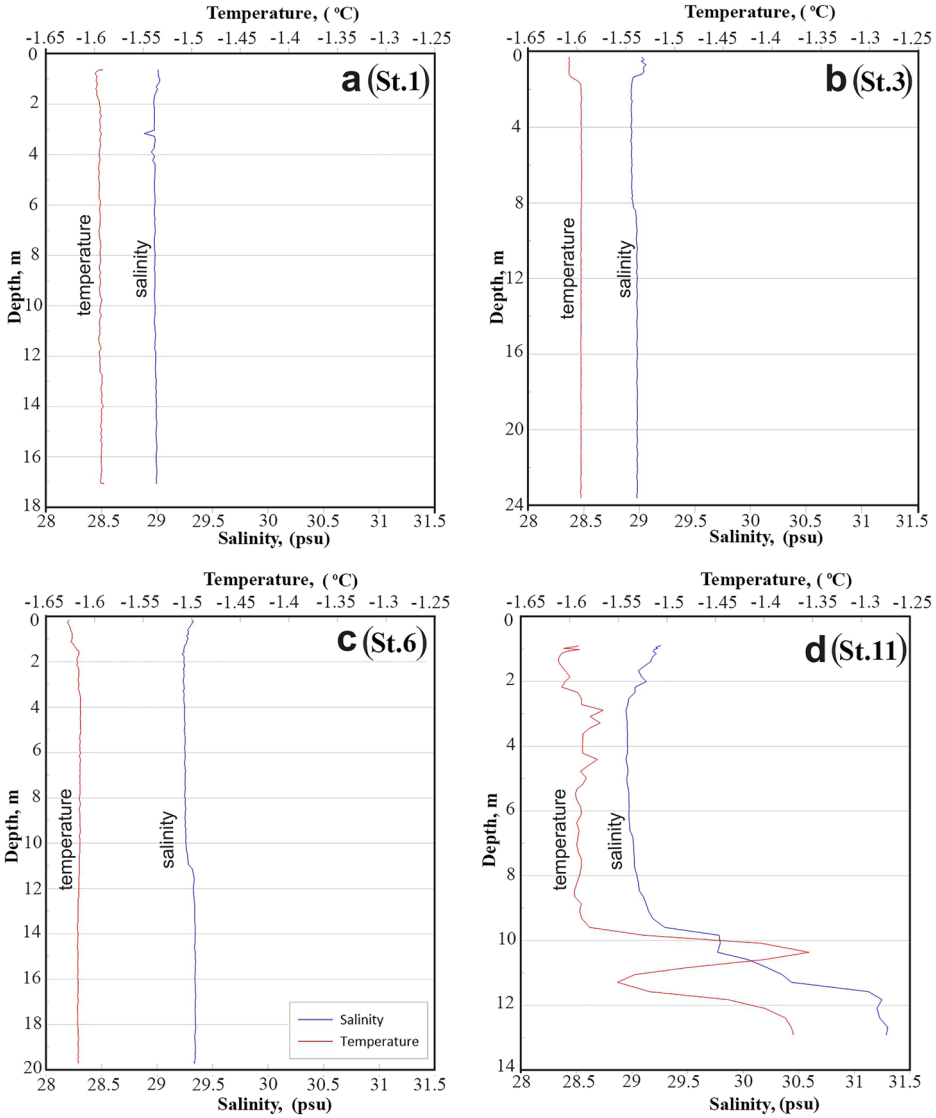

Fig. 3 | Temperature and salinity vertical profiles of the winter water column in Chaun Bay completed during April 2023. a Temperature and salinity vertical profiles at station 1. **b** Temperature and salinity vertical profiles at station 3. **c** Temperature and salinity vertical profiles at station 6. **d** Temperature and salinity vertical profiles at station number 11.

derived salinity distribution at 8 meters deep (Supplementary Fig. 15). Comparison of this map with the salinity distribution measured by the Smart Fish robotic system shows common trends like the salinity maximums near Cape Naglyoynyn and the Chaun River mouth, however it also reveals a new salinity peak slightly southwest of the one near the Pevek Peninsula on the CTD-derived distribution map (Supplementary Fig. 15). Profiling with the robotic system could not have missed this anomaly since its route overlapped this location (Supplementary Fig. 2). One possible explanation for this discrepancy is the different time durations of the two CTD-profiling methods used. The continuous profiling using the Smart Fish robotic system was carried out over two days in the beginning of our expedition; in contrast, traditional CTD-profiling and sampling required more time per station and was therefore conducted over 8 days. Moreover, the northwestern part of the bay, where the eddy core presumably shifted, was sampled using CTD only at the very end of the expedition period, 6 days after the continuous probing (Supplementary Fig. 14). This also likely caused the distortion of the 'radium age' along the AC route, as water samples for radium measurements were collected with Niskin bottles concurrently with the CTD sampling (Supplementary Fig. 14). The eddies observed during our studies, including the main cyclonic and an anticyclonic one in the southern part of the bay, are visible on the satellite imagery taken several months before our expedition, during summer (Fig. 2d). This suggests a quasi-stationary nature of these eddies that likely form due to the meandering interaction of low-density coastal Arctic water and high-density saline groundwater[13,14] at the surface front. However, longer observations are required to confirm these dynamics, as well as the formation process of the cyclonic eddy core from saline waters introduced via SGD.

In addition to naturally occurring radium isotopes, water at the SGD site near Cape Naglyoynyn was highly enriched with dissolved metals (Supplementary Table 3; Supplementary Fig. 16), further supporting the presence of submarine groundwater, which is typically rich in those elements[15]. Conversely, the lower concentrations of dissolved metals at the mouth of the Chaun River likely result from the different hydrogeological conditions at this location compared to the other SGD site. As these waters move eastward and northward, following the cyclonic circulation pattern, concentrations decrease due to oxidation processes facilitated by an inflow of oxygen-rich waters from the ESS and the formation of interacting colloids (Supplementary Table 1; Fig. 2c). These mixed iron (Fe) and manganese (Mn) colloids with adsorbed metals precipitate onto hard-rock surfaces as poorly crystalline or amorphous oxyhydroxides, potentially catalyzed by bacterial activity, resulting in the formation of extensive ferromanganese formations, which covered the seafloor across several central and near-shore areas of the bay (Supplementary Table 4; Supplementary Fig. 17). The Fe/Mn ratio in these formations near Cape Naglyoynyn (1.54) suggests a mixed hydrogenetic and hydrothermal genesis, which is typically characterized by values between 1 and 3, and more commonly between 1.3 and 1.8[16]. Chaun Bay also showed the highest activity concentrations of ^{226}Ra, ^{232}Th, and ^{40}K

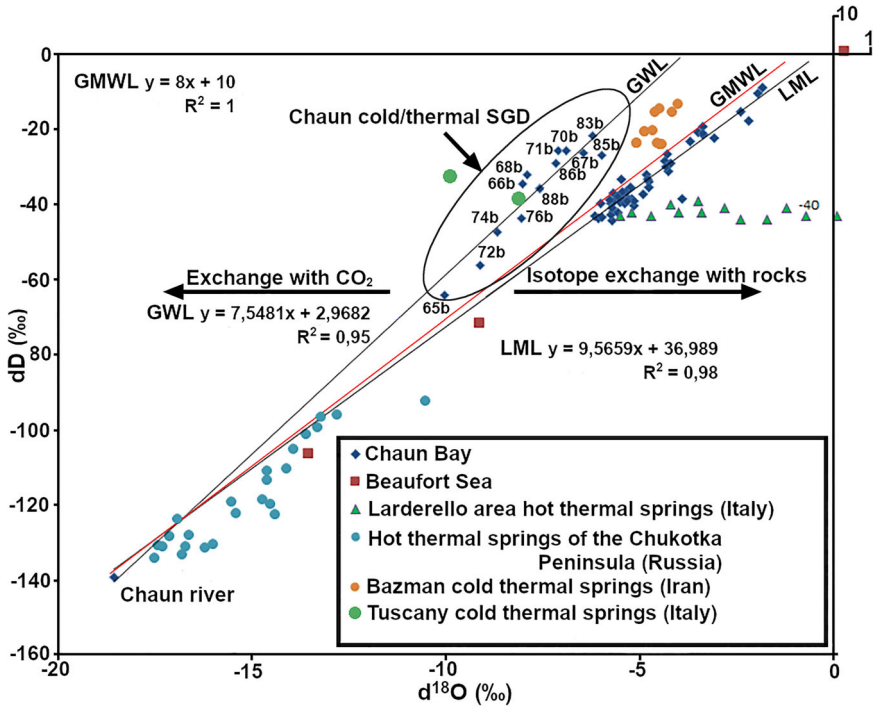

Fig. 4 | The relationship between hydrogen and oxygen isotope values for samples collected in Chaun Bay during October 2020. Boxplot showing the $\delta^{18}O$ versus δD in water samples from Chaun Bay as well as hydrothermal waters from different regions of the planet and seawater from the Beaufort Sea. The local water line (LWL) is represented with black, the global meteoric water line (GMWL)[68] with red, while a line representing submarine cold/thermal waters is shown in gray as GWL. Arrows indicate isotope exchange. Data from Supplementary Table 6.

radionuclides in marine sediments compared to the entire ESS shelf[7,17], further support the existence of a powerful SGD source.

Waters in the SGD locations were also rich in nutrients, which is another typical feature of SGD globally[18]. While high ammonium and phosphorus levels were observed near Cape Naglyoynyn, the nutrient concentrations at the Chaun River mouth were around baseline (Supplementary Table 5; Supplementary Figs. 18, 19), likely also as a result of the different hydrogeological conditions of these two areas. The high silicon concentrations near the Pevek Peninsula were most likely due to runoff from the Chaun River, as maximum silicon values were observed at the river mouth (Supplementary Table 5). The relationship between DIN/DIP and salinity (Supplementary Fig. 20) showed anomalously low values near Cape Naglyoynyn, including at Stations 71 and 81, indicating a significant inorganic phosphorus influx with groundwater, while the elevated DIN/DIP ratio near Pevek Town were attributed to inorganic nitrogen compounds, likely from domestic effluents. The areas influenced by SGD were also clearly marked by reduced pH values (Supplementary Table 1; Supplementary Fig. 21). During the observation period, the surface waters predominantly acted as a sink for atmospheric carbon dioxide. The partial pressure of CO_2 was also low due to intensive cooling, as evidenced by water temperatures in the surface and near-bottom layers (Supplementary Table 1; Supplementary Fig. 5). As the temperature drops, the solubility of carbon dioxide increases, which would typically result in lower pCO_2 values during the autumn-winter cooling period, expected to be below the atmospheric equilibrium value of 400 µatm. However, in SGD-affected areas, a drop in pH values was also observed in the surface water layer (Supplementary Table 1; Supplementary Fig. 21).

The high water temperatures relative to surrounding areas, even in winter under-ice conditions, along with elevated activity levels of naturally occurring radium isotopes, metal concentrations, and pCO_2, suggest a hydrothermal origin of the identified SGD locations. This conclusion is further supported by $\delta^{18}O$ and δD data, which show that the slope of the Groundwater Line (GWL) in near-bottom water at these sites is much steeper than that of both global meteoric water line (GMWL) and local water line (LWL) (Fig. 4), and is similar to values observed in cold/thermal springs in Italy and Iran[19,20]. The waters in SGD locations were markedly depleted of ^{18}O isotopes, while their deuterium levels align with those of a marine source (Fig. 5), which, together with their high salinity, suggests that these waters are of marine origin, most likely originating from the deep-water areas of the ESS. A potential mechanism of their ingress may be the convective circulation of sea water[21] that seeps through its feed zone on the ESS shelf, heats up over a magma pocket, becomes buoyant, and rises to the surface of Chaun Bay seafloor. Notably, the water samples depleted of ^{18}O isotopes were only observed at the seabed (Fig. 5a, d), arranged in a pattern resembling the letter 'C', indicative of an almost closed eddy and emphasizing the effects of cyclonic vorticity. This leads to convergence of warm water against the upwelling at subsurface around the eddy core[22], clearly seen on the thermohaline sections (Supplementary Figs. 6–8), forcing warm waters downward towards the near-bottom horizon (Fig. 5d).

Geomagnetic surveys identified a positive linear magnetic anomaly in the southern part of the bay, with a heterogenous internal structure marked by local maxima ranging from 10–23 nT in amplitude. This anomaly broadens sigificantly in the sub-meridian direction near Cape Naglyoynyn and the Chaun River mouth closures (Fig. 6). Quantitative analysis shows that this magnetic anomaly originates from a magnetized volcanic body in the form of a vertical intrusion about 10 km wide, expanding to 35 km in the west near Cape Naglyoynyn (Fig. 6). Volcanic rock is known to have strong magnetic properties due to its considerable iron and titanium oxide content[23], which is consistent with the high dissolved iron and titanium concentrations in SGD locations near Cape Naglyoynyn (Supplementary Table 3; Supplementary Fig. 16). Moreover, magnetotelluric data show the presence of areas with very low resistivity (< 50 Ohm m) at depths of 5–50 km[24] (Supplementary Fig. 22). Such low resistivity bulk is a typical indication of hot molten rocks or a magma chamber[25]. From the data above we hypothesize that this magnetic body, situated along a diagonally directed linear destructive zone, is the most likely heat source of the stable convective groundwater circulation in the sedimentary strata above it. In addition to being a heat source, these volcanogenic structures may also emit CO_2, which interacts with water at approximately +25 °C and exchanges with stable oxygen isotopes, thereby reducing ^{18}O concentration in the groundwater[19]. This process would explain the observed shift in the $\delta^{18}O$ to δD ratio in the GWL relative to GMWL and LWL (Fig. 4). This conclusion is also supported by the high levels of dissolved pCO_2 in near-bottom waters at the thermal SGD locations (Supplementary Table 1; Supplementary Fig. 21).

To detect a possible thermal SGD effect on the temperature regime of Chaun Bay, heat budget calculations were performed using two

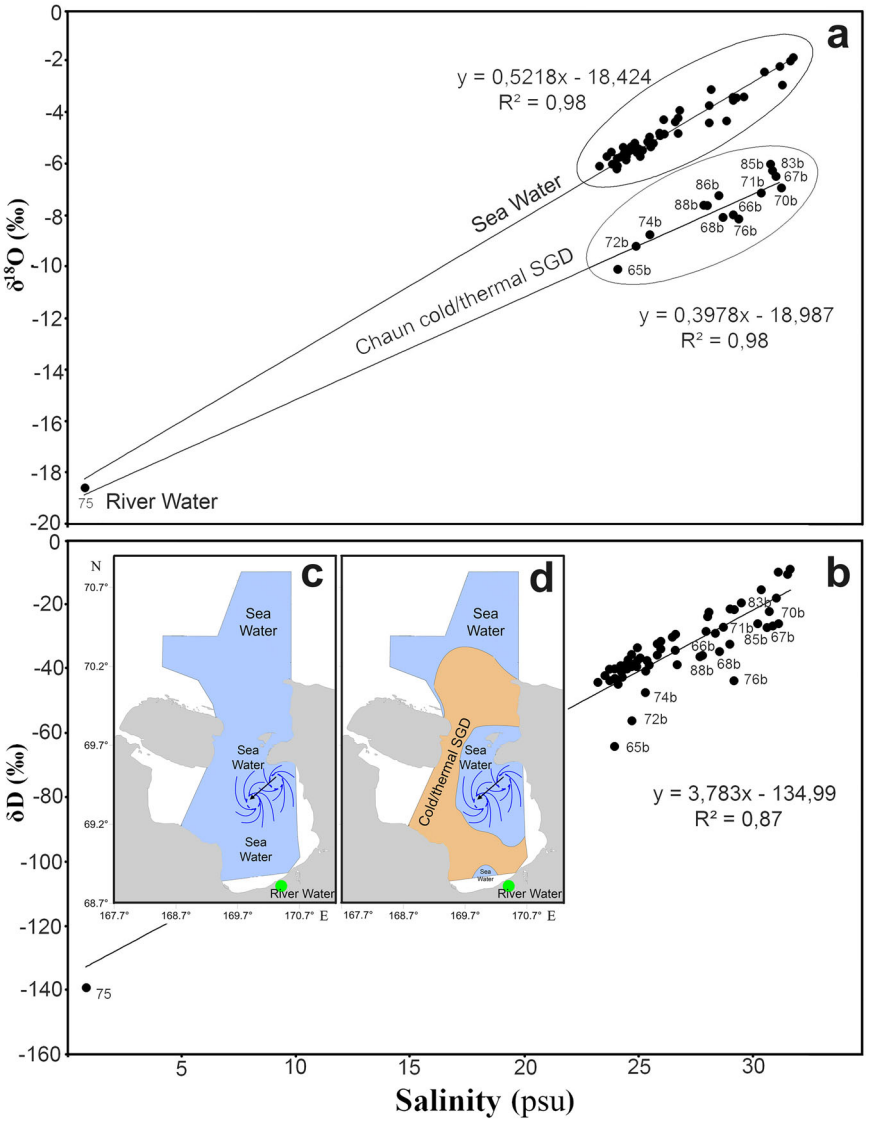

Fig. 5 | The relationship between salinity and hydrogen, oxygen isotope values in water samples from Chaun Bay collected during October 2020. **a** $\delta^{18}O$ versus salinity. **b** δD versus salinity. Shown the location influenced by the eddy core, as well as a conceptual representation of sea water and cold/thermal groundwater in study area, according to $\delta^{18}O$ vs. salinity data for surface horizon (**c**) and bottom horizon (**d**). The blue arrows show convergent flow around eddy core. The black arrow shows the direction of eddy movement. Salinity data from Supplementary Table 1. $\delta^{18}O$ and δD data from Supplementary Table 6.

oceanographic reanalyses – GLORYS12v1[26] and Global Ocean Forecasting System (GOFS) 3.1[27], as well as the atmospheric reanalysis ECMWF ERA5[28]. The results obtained reveal an inconsistency in the heat balance of Chaun Bay: for both oceanographic reanalyses the total heat flow across the boundaries was not equal to the increase in internal energy (Table 1). This discrepancy indicates the presence of an additional heat source not taken into account by GLORYS12v1 and GOFS3.1 models, which rely only on oceanographic data assimilation. Assimilation of seawater temperature is a fictitious, therefore, unaccounted source of heat in the oceanographic model equations. Consequently, this confirms the significant influence of submarine thermal SGD on the temperature regime of Chaun Bay and demonstrates the need for further assessments. Estimating the bottom heat flux associated with geothermal sources is a challengling task that cannot be solved by simply estimating the heat balance, but we attempt to estimate it indirectly. The average temperature difference between the results of CTD measurements and the data of the GOFS3.1 oceanographic reanalysis was ΔT = 0.3 °C. The change in internal heat storage that corresponds to this temperature deviation is as follows:

$$\Delta H_{Storage} = c_p \cdot \rho \cdot V \cdot \Delta T = 1.09 \cdot 10^{17} J \quad (1)$$

Since this difference in temperature was observed throughout the entire period of the expedition, we assume that this temperature was established during the October. Therefore the rate of change of internal heat storage can be estimated as:

$$\Delta H_{Storage} = 1.09 \cdot 10^{17}/(30 \cdot 24 \cdot 60 \cdot 60) = 4.21 \cdot 10^{10} J/\,\mathrm{sec} \quad (2)$$

and the heat flux from a geothermal source will equal to:

$$c_p \cdot \rho \cdot \Delta V \cdot \Delta T = 4.21 \cdot 10^{10} \Rightarrow \Delta V \cdot \Delta T = 9790 \quad (3)$$

If we assume the average temperature of a geothermal source to be ΔT = 50 °C, then the volume transport of geothermal source will amount to:

$$\Delta V = 9750/50 = 195\ \mathrm{m^3 s^{-1}} \quad (4)$$

Thus, the comparison of the CTD-data with the GOFS3.1 gives an approximate volume transport of geothermal source of about 200 $m^3\ s^{-1}$. By analogy, for the CTD-data with GLORYS12v1 and the temperature deviation ΔT = 0.1 °C we estimate the volume transport of geothermal source to be about 60 $m^3\ s^{-1}$.

Chaun Bay sharply stands out from the broader ESS shelf due to the resemblance of some aspects of its benthic and zooplankton communities to those of the southern Chukchi Sea and even the North Pacific Ocean (Fig. 1). The structure of both benthic and zooplankton communities in Chaun Bay

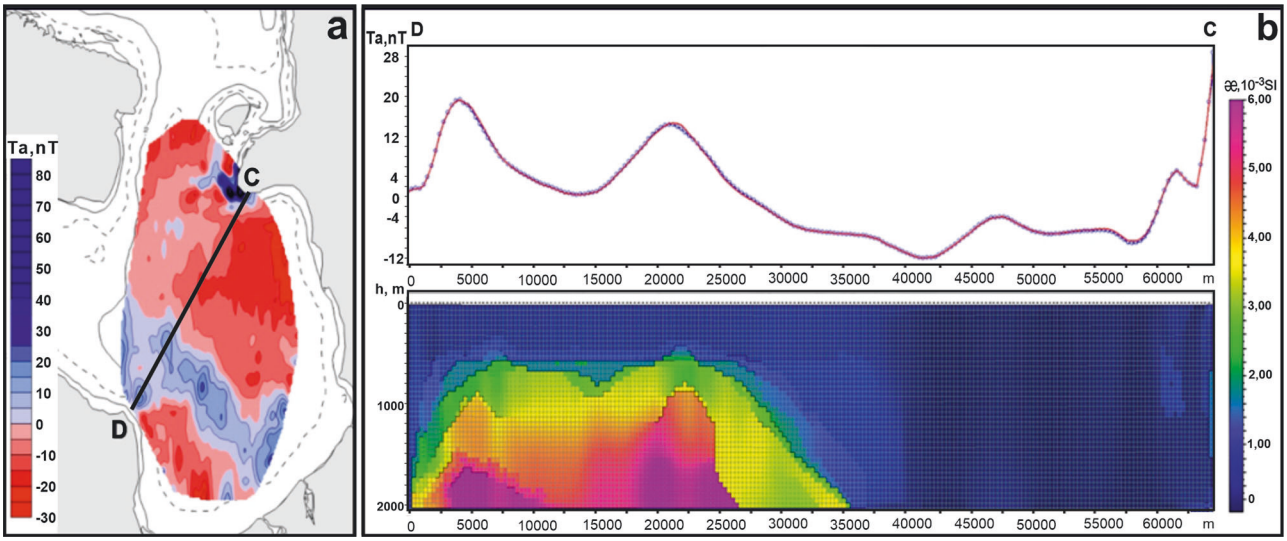

Fig. 6 | The structure of the upper part of the Earth's crust of Chaun Bay according to the results of geomagnetic studies. a The abnormal magnetic field of Chaun Bay in the form Ta = T - Tn – δT, where T - the observed geomagnetic field, Tn - the normal field, δT - the field of variations. D-C position in plan of the quantitative interpretation profile. **b** Quantitative interpretation abnormal magnetic field in a two-dimensional version along the D - C profile. The upper part of the picture is an abnormal magnetic field (Ta). The measurement results are shown in blue. The calculation results are shown in red. In the lower part of the picture, the color shows the discrete distribution of magnetic masses in the upper part of the earth's crust in accordance with the scale of magnetic susceptibility. The magnetization of the model medium is calculated based on magnetic susceptibility. The most intensely magnetized areas correspond to the magmatic body of the main composition, the least magnetized areas correspond to sedimentary rocks.

Table 1 | Monthly amount of heat gained/lost by the waters of Chaun Bay for 2019 in PetaJoule

Month	Heat storage rate		Heat flux through vertical open boundary		Heat flux due to ice		Heat flux through surface	
	GLORYS12v1	GOFS3.1	GLORYS12v1	GOFS3	GLORYS12v1	GOFS3	ECMWF ERA5	GOFS3
1	−23.81	−8.47	1.51	0.00	616.11	395.19	−485.23	0.00
2	−8.08	−7.70	0.15	0.03	647.64	424.32	−339.00	0.00
3	11.48	−0.69	0.86	0.07	536.32	420.72	−114.42	0.00
4	45.85	0.46	1.46	0.73	−701.08	4.93	166.06	0.00
5	60.06	20.30	5.12	−0.12	−28.14	−301.40	866.78	0.00
6	775.65	415.72	7.78	6.73	−3218.24	−1967.5	2239.49	0.01
7	462.89	1643.98	−13.32	−22.47	−579.99	−1041.4	1218.06	0.36
8	1445.34	178.27	−28.14	−0.03	0.00	0.00	715.29	0.05
9	−1480.68	−1214.30	33.46	2.02	0.00	0.00	−257.51	−0.39
10	−1350.10	−1024.44	9.43	2.66	1420.62	825.35	−788.20	−0.31
11	−18.31	−0.90	1.45	0.01	897.55	757.48	−694.77	0.00
12	−9.40	−4.18	0.83	0.01	632.71	848.22	−504.92	0.00
Total	−89.11	−1.94	20.60	−10.36	223.50	365.79	2021.64	−0.30

were largely governed by the distribution of thermohaline properties across the bay. In its central part, the benthic epi- and infauna were typical of Siberian Arctic estuaries, with abundance ranging between 200 and 908 ind. m^{-2}, biomass between 5 and 40 g m^{-2}, and species diversity between 11 and 14 species per Van Veen grab sample (21 species observed in total) (Fig. 7). By comparison, in the soft-bottom benthic communities of the ESS shelf, the number of species typically does not exceed 30, and their mean abundance and biomass falls between 820 and 1070 ind. m^{-2} and 58.3–78 g m^{-2}, respectively[29]. In contrast, near Cape Naglyoynyn, south of the Pevek Peninsula, and near the Chaun River mouth, both abundance and species diversity significantly exceeded these values, even in fine sediments: abundance ranged between 3433 and 12,292 ind. m^{-2}, biomass between 161 and 363 g m^{-2}, and number of species reached 29–52 species per grab sample, and up to 55 species per trawl haul (Fig. 7). In total, we observed 102 species in the sediment (grab) samples and 143 species in the trawl samples. The communities were typically dominated by the molluscs *Astarte montagui* and *Astarte borealis*. The sizes of the dominant mollusc species (*Astarte* spp., *Portlandia arctica, Ennucula tenuis*) significantly (up to two times) exceeded those in the center of the bay.

The influence of thermal waters, which rise and form a layer without contacting the seafloor (Supplementary Table 1; Fig. 2a; Supplementary Figs. 6, 9), on benthic communities is limited to a small area. However, their indirect effects are far-reaching. The high nutrient levels and higher temperature of the layer formed by thermal waters result in active phytoplankton production (Fig. 8c), and these areas (Cape Naglyoynyn and the Chaun River mouth) were characterised by the highest zooplankton biomass (Fig. 8a, b). Chlorophyll–a concentrations in the SGD locations reached up to 9.4 mg/m^3 in the surface layer and up to 7.4 mg m^{-3} in the bottom layer, values comparable to those observed in the highly-productive Chukchi and Barents Sea regions during the spring bloom[30]. By comparison,

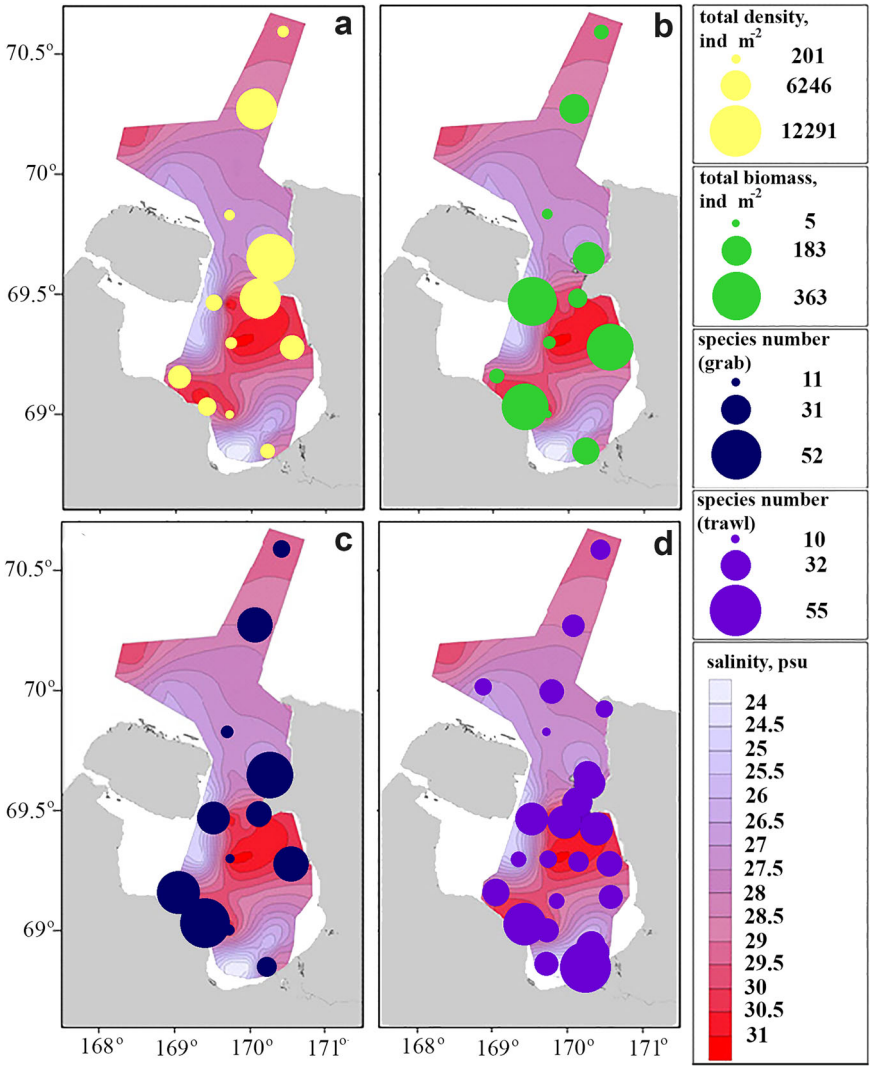

Fig. 7 | Spatial distribution of zoobenthos in Chaun Bay collected during October 2020. **a** Abundance distribution. **b** Biomass distribution. **c** Species diversity in grab. **d** Species diversity in trawl. The increased salinity of the bottom water is given as an indicator of transformed hydrothermal waters.

chlorophyll in other interior Arctic Seas, including the ESS[31], rarely exceed 1 mg m^{-3} [32]. Organic matter produced in these hydrothermal areas is partially retained within small zones and partially distributed to the Pevek Peninsula by eddy currents (Fig. 2; Supplementary Figs. 6, 7, 14). The resulting convergence of warm water around the eddy core (Fig. 5d) can, in turn, deliver food and heat to the near-bottom layer, where we observed the maximum benthic biomass and species diversity (Fig. 7).

The high salinity (29–31 psu), which exceeds even that of the adjacent part of the ESS (25–29 psu), results in a high percentage of marine species unusual for an estuary — including those of Pacific origin, which have also been noted by previous studies[2]. This salinity profile also leads to the absence of typical Arctic brackish-water zooplankton species (*Drepanopus bungei, Pseudocalanus major*, and *Limnocalanus macrurus*) in the bay. At the mouth of the Chaun River (one of the SGD locations), where the highest influence of freshwater might be expected, high nutrient concentrations and increased salinity in the near-bottom layer were observed instead (Fig. 2; Supplementary Figs. 6, 7).

A notable feature of the benthic communities of Chaun Bay was the presence of species not typical for the Siberian Arctic (Fig. 1). The most spectacular example were the colonies of the mussel *Mytilus trossulus*[33], which have been observed in the shallow near-shore waters of the western and eastern parts of Chaun Bay[2] and were amply represented in our samples from depths greater than 10 m near Cape Naglyoynyn and at the mouth of the Chaun River (Supplementary Fig. 30). Similarly, we observed the boreal bryozoans *Einhornia crustulenta* and *Tegella anguloavicularis*, cumaceans *Leucon (Leucon) kobjakovae* (2), and the hermit crab *Pagurus capillatus* (Fig. 1, Supplementary Fig. 31), which is typical of Far Eastern seas and the southeast of the Chukchi Sea[34–36], but has never been observed in the Siberian Arctic prior to our expedition. Increased temperatures in the water column and high salinity also supported populations of the euphausiids (krill) *Thysanoessa* spp. (Supplementary Figs. 32, 33), which are typically absent in the Arctic Ocean except for regions influenced by Atlantic or Pacific inflow[37]. Euphausiids have been previously observed on the ESS shelf[38–40] together with aggregations of bowhead whales, which were presumably feeding on them[40], but it has always been assumed that the euphausiids represent expatriated individuals advected from the North Pacific Ocean[39]. However, their large quantities were also observed during the 2023 winter expedition under 1,5 m ice, although no quantitative sampling could be done due to logistical limitations. This observation strongly suggests that *Thysanoessa* spp. in this region are not advected drifters from the Chukchi Sea, but rather represent an independent, permanent population in this area. On the contrary, the Chaun Bay population may be a source of euphausiids for the broader ESS shelf, as they are active swimmers and can cover large horizontal distances, following the food conditions. Curiously enough, the expedition of the USSR Academy of Sciences' Zoological Institute[2] organized in the late 1980s did not register euphausiids in Chaun Bay. This may indicate that these animals were introduced to the bay and established a permanent population there within last 30 years; alternatively, it could be a sampling bias due to the fact that euphausiids are notoriously hard to capture using small plankton nets.

In summary, the unique combination of volcanogenic structures, a strong flow of saline groundwater supplying heat and nutrients, and the

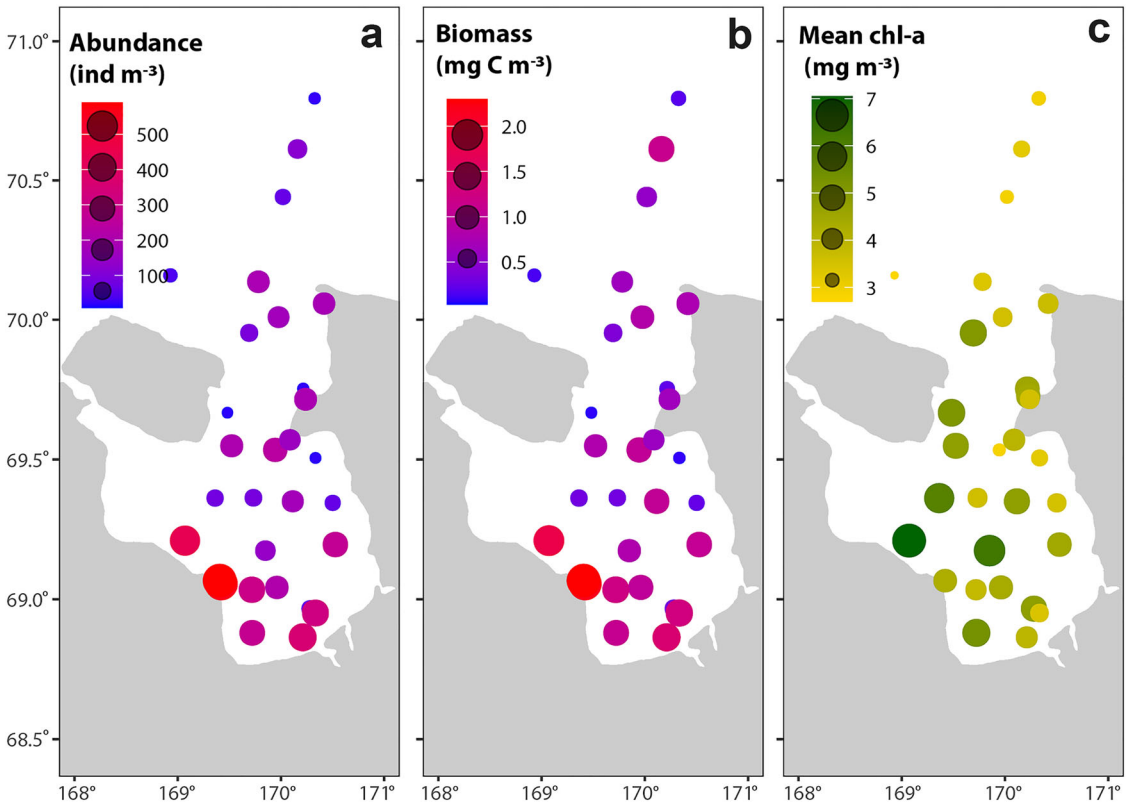

Fig. 8 | Spatial distribution of mesozooplankton and mean chlorophyll–a in Chaun Bay collected during October 2020. a Abundance distribution of the mesozooplankton. **b** Biomass distribution of the mesozooplankton. **c** Mean chlorophyll–a distribution.

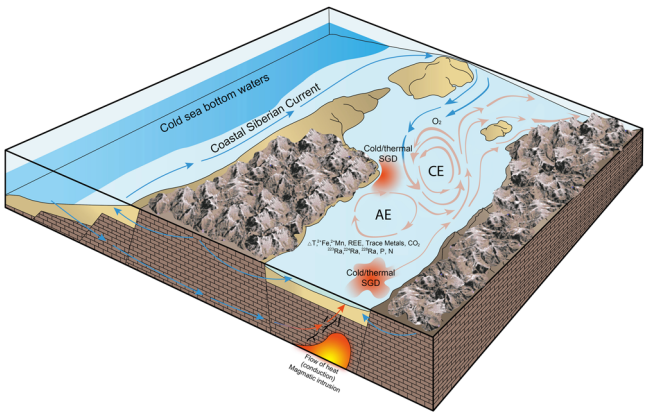

Fig. 9 | Conceptual representation showing the mechanism for the formation and maintenance of the unique "Arctic oasis" in Chaun Bay. Blue arrows show the movement of water from the East Siberian Sea, red arrows show the movement of cold/thermal submarine groundwater, red spots show cold/thermal submarine groundwater discharge (SGD) location, AE anticyclonic eddy, CE cyclonic eddy. Opposite the blue arrow shows dissolved oxygen supplied from the East Siberian Sea to Chaun Bay. Near cold/thermal SGD location release of some chemicals affecting the ecosystem of Chaun Bay is shown.

partially enclosed structure of the bay with a cyclonic circulation has led to the emergence and long-term maintenance of a unique 'Arctic oasis'. This oasis serves as a shelter for rich biological communities that include boreal species not found elsewhere in the Arctic outside of regions heavily influenced by Atlantic or Pacific inflow (Fig. 9). Chaun Bay can be likened to a 'saucepan with soup', gently simmering on low heat (volcanogenic structures) while being intensively stirred by a spoon (cyclonic eddy), to which an 'invisible' cook (SGD) continuously adds ingredients like nutrients, dissolved metals and salt. Meanwhile, an almost closed eddy at the seabed retains most of the heat while drawing oxygen-enriched surface waters downwards to the seabed around the eddy core. As a result, Chaun Bay serves as a refuge for thermophilic species in eastern Siberia and may facilitate the further expansion of boreal species into the Arctic with warming climate, as suggested by our observations of the euphausiids *Thysanoessa* spp. Moreover, Chaun Bay itself may play a previously unrecognized role in warming the Siberian Arctic by ventilating the waters of the adjacent East Siberian Sea shelf.

Methods

Fieldwork

Chaun Bay, where this study was conducted, is located in the southeast of the East-Siberian shelf (Fig. 1). This is a shallow bay, the depth of which does not exceed 30 meters. The bay is 140 km long and has a northward orientation. Its maximum width is 110 km. Its mouth is defined by Cape Shelagsky at the end of the Shelag Range on the east side and an unnamed part of Ayon Island on the west. It narrows where its eastern Pevek Peninsula approaches Ayon Island. Many small rivers flow into the bay (Chaun River, Ichuveyem River, Palyavaam River, Lelyuveyem River, and Pucheveyem River), and their total annual flow does not exceed 9 km [32].

Hydrological surveys and water sampling

The water column's thermohaline characteristics were measured using a Conductivity-Temperature-Depth (CTD) sensor package (Sea Bird 19Plus) at 48 stations during October 2020 onboard the Research Vessel *Akademik Oparin*. The CTD was incorporated into a water sampler composed of 12 Niskin bottles. Water samples were taken at the surface (3.5–4 m depth), at the bottom (1–2.5 m from the bottom), and at the intermediate horizons (at deep stations). The salinity measurements obtained by the CTD were calibrated by direct salinity measurements via a salinometer.

Hydrological surveys via underwater profiling of "Smart Fish"

The towed robotic system "Smart Fish" was designed specifically for this expedition in order to study the water column and bottom sediments in three different modes (Supplementary Figs. 3, 4). This array incorporated pressure, electrical conductivity, temperature (ACTW-CAR/CAD, JFE Advantech Co., Ltd., Japan), and dissolved oxygen (RINCO IID ARO05/1/2/5-CAR/CAD, JFE Advantech Co., Ltd., Japan) sensors, as well as a gamma spectrometer in a special capsule made of polymer materials (not used in our expedition). This instrument was used to collect continuous thermohaline measurements at a depth of 6-8 meters (mode A) along a route across the entire bay (Supplementary Fig. 2). Registration of data, time, and coordinates was performed every 2 seconds via a mobile PC onboard the vessel.

Radium isotope measurements

Water samples for radium isotope measurements in seawater were collected at different depths using Niskin bottles (60–100 L). These samples were filtered through 1 mm polypropylene cartridges and MnO_2 fiber at a flow rate of no more than 1 L/min, achieving a radium extraction efficiency of at least 97%[41]. The ^{224}Ra and ^{223}Ra isotopes were quantified using the delayed coincidence scintillation counting method[42]. For the calculation of ^{224}Ra and ^{223}Ra counts, the chance coincidence correction was applied, rather than the alternative procedure based on total counts[43]. The associated uncertainties of the measurements were estimated according to Garcia-Solsona et al.[43]. After the initial ^{224}Ra and ^{223}Ra measurements in the research vessel laboratory, Mn fibers containing radium samples were aged for 2 to 6 weeks. This aging process allowed the initial excess ^{224}Ra (ex^{224}Ra) activity to reach secular equilibrium with the ^{228}Th also absorbed on the Mn fiber. The samples were then analyzed again to determine ^{228}Th levels to correct for supported ^{224}Ra[42,44]. After about 100 days, the samples were analyzed a third time to measure ^{227}Ac (actinium)-supported ^{223}Ra, though ^{227}Ac activity was below the detection limit and thus considered negligible.

For long-lived ^{228}Ra isotope analysis, the Mn fiber was re-analyzed using the RaDeCC system approximately 6–12 months after sample collection. This delay allowed for the growth of ^{228}Th from its precursor, ^{228}Ra (T1/2 = 5.75 years). Corrections were made for the decay of ^{228}Th initially coated on the Mn fibers, and ^{228}Ra activity was estimated as described in Moore[42]. We calibrated the RaDeCC systems for ^{224}Ra, ^{223}Ra, and ^{228}Ra measurements using ^{232}Th standards as described by Moore and Cai[45]. The average statistical counting error was ± 3.1 % (range = ± 0.52 – 8.99 %) for ^{224}Ra, ± 16.8 % (range = ± 5.9 – 37.6 %) for ^{223}Ra, and ± 10.5 % (range = ± 5.4 – 27.7 %) for ^{228}Ra.

Calculation of SGD residence time based on radium isotopes

The groundwater discharged from bottom sediments into the water column maintains the same ^{224}Ra/^{223}Ra activity ratio as the pore water; this activity ratio is defined as the initial ratio ([^{224}Ra/^{223}Ra]init) or the ratio of ^{224}Ra/^{223}Ra defined at $t = 0$ days[46,47]. This initial activity ratio reflects the constant decay of parent isotopes in the bottom sediments. As radium–enriched pore water (groundwater) enters the seawater, the activity ratio begins to change to reflect the different decay rate constants of the two isotopes. Because ^{224}Ra has a greater decay constant than ^{223}Ra ($\lambda 224 = 0.189$ day^{-1} and $\lambda 223 = 0.0606$ day^{-1}, respectively), the activity ratio will decrease systematically with time, providing a radium–derived age[46]. It is important to consider potential radium contributions from other sources post-initial enrichment to effectively model radium ages[44,48].

In order to calculate the growth of the "radium age" in the sampled waters, we used Eq. (1) proposed by Moore[49],

$$t = \frac{\ln\left[\frac{^{224}\mathrm{Ra}}{^{223}\mathrm{Ra}}\right] - \ln\left[\frac{^{224}\mathrm{Ra}}{^{223}\mathrm{Ra}}\right]_{init}}{\lambda_{223} - \lambda_{224}} \quad (5)$$

where t represents time (days), [^{224}Ra/^{223}Ra] is the calculated activity ratio in the water sample, [^{224}Ra/^{223}Ra]init is the calculated activity ratio in the radium–enriched endmember, and $\lambda 224$ and $\lambda 223$ represent the respective ^{224}Ra and ^{223}Ra decay constants of 0.189 day^{-1} and 0.0606 day^{-1}. For [^{224}Ra/^{223}Ra]init we used the ^{224}Ra/^{223}Ra activity ratio (26.4) measured in the submarine groundwater of the Laptev Sea[11].

δ^{18}O and δD measurements

Isotopic signature measurements of water were conducted by a *Picarro L −2130-i* laser analyzer. Interlaboratory reference samples were used as standards, adhering to IAEA V-SMOW-2, GIPS, and SLAP. Reproducibility of the measurements was 0.1‰ for oxygen δ^{18}O and 0.5‰ for δD.

Determination of trace elements by plasma-mass spectrometry

Trace element content in the water samples was measured using inductively coupled plasma mass spectrometry on an Agilent 7700 x spectrometer (Agilent Techn., USA) equipped with a concentric nebulizer, cyclonic spray chamber, quartz torch, and octupole reaction system. The ICP-MS was optimized daily to reach manufacturer-recommended sensitivity and stability. The standard sample introduction system was used with a glass concentric nebulizer, quartz spray chamber, and quartz torch (2.5 mm internal diameter injector). The calibration standards were prepared in an acid matrix of 1% HNO3 and 0.5% HCl to ensure the stability of elements Ag, Sb, and Hg.

Elemental analysis of ferromanganese nodule samples

Concentrations of SiO_2, Al_2O_3, Fe_2O_3, TiO_2, MgO, Na_2O, K_2O, CaO, MnO, P_2O_5, Cl, Cr, S, Ni, Cu, Zn, Rb, Sr, Ba, Y, and Zr in ferromanganese nodule samples were measured using energy dispersive X-ray fluorescence (EDXRF) on an EDX-800-HS analyzer (Shimadzu, Japan). Before the procedure, freeze-dried samples were finely pulverized with a Pulverisette 7 planetary mill (Fritsch, Germany) at 670 rpm for 10 min, then sieved and quartered. For measurement, samples were converted into tablets with a diameter of 20 mm using a manual press with pressure 30 MPa, sample weight 2 g, and binding agent H_3BO_3 (1 g of sample to 0.5 g of H_3BO_3). The source of excitation was an X–ray tube with an Rh anode. The exposure time of the sample was 100 s in each energy channel. The samples SRM 2702 (Inorganics in Marine Sediment) and SRM 2703 (Sediment for Solid Sampling (Small Sample) Analytical Techniques) were used as references. The analytical reproducibility of the measurements was estimated at ± 5% for elements with a concentration > 1% and ±10% for elements with a concentration < 1% in the sample.

Nutrients

Ammonium concentration was determined using the indophenol method. Nitrates, nitrites, dissolved silicates (DSi), and dissolved inorganic phosphorus (DIP) were measured using standard colorimetric methods. The nutrient analysis followed methods described in Grasshoff et al.[50]. Ammonium, nitrate, and nitrite concentrations were summed to determine the total dissolved inorganic nitrogen (DIN). Total phosphorus and nitrogen were determined on a SKALAR SAN + + automated analyzer (Skalar, the Netherlands). The detection limit was 0.01 μmol L^{-1} for phosphate and nitrite, and 0.02 μmol L^{-1} for silicate. Analytical error was < 10% for all nutrients, based on duplicate samples analyzed every ten samples.

Total alkalinity (TA)

Samples for TA were analyzed using a titration indication method in which 25 ml of seawater was titrated with 0.02 N HCl in an open cell according to the Bruevich method[51]. Measurements were performed at 20 °C, where the temperature in the cell was controlled to be within 0.1 °C. In 2000, the North Pacific Marine Science Organization (PICES) group working on North Pacific CO_2 performed a TA intercalibration in seawater using certified reference materials (CRMs). The results showed that the TA values obtained by the Bruevich method are in agreement with the standard solution, within ±1 μmol kg^{-1} when state-of-the-art analytical practice is applied. During the 2016 cruise, TA measurements were performed with a precision of ±2 μmol kg^{-1}, controlled by calibration using CRMs supplied by A. Dickson of the Scripps Institution of Oceanography in the USA.

pH

A potentiometric method was applied to determine pH using a cell without a liquid junction[52] and reported on the total hydrogen ion concentration scale[53]. The precision of pH measurements was about 0.004 pH units.

Partial pressure of carbon dioxide (pCO_2) and calcium carbonate saturation state (Ω) calculations

At CTD stations, the pCO_2 and saturation states of the carbonate mineral aragonite Ω_{Ar} were calculated from the pH and TA using the CO2SYS program developed by Lewis and Wallace[54]. Carbonic acid dissociation constants (i.e., pK_1 and pK_2) from Mehrbach et al.[55] as refit by Dickson and Millero[56] were used for the computation, as well as the dissociation constants for HSO_4[57] Ω_{Ar} is defined as the ratio of the ion product of carbonate and calcium concentrations to the experimental solubility product, K_{sp}, (i.e. $\Omega_{Ar} = [Ca^{2+}] \times [CO_3^{2-}]/K_{sp}$)[58].

Geomagnetic survey collection and processing

Geomagnetic field full vector module (T) measurements were made by the MPMG-04 marine towed proton magnetometer developed in Russia (IZMIRAN). The geo-referencing of the measurement points was made by GPS Map 420 S (Garmin, USA), which was improved by accounting for nature-based geomagnetic field variations based on synchronous magnetovariational measurements at the northeast coast of Chaun Bay. An Overhauser MMPOS−1 magnetometer (Russia) was used to register variations of the geomagnetic field with a period of 4 s^{-1}.

The observed geomagnetic field (T) was counted as the sum of the normal field (Tn), abnormal field (Ta), and the field of variations (δT): T = Tn + Ta + δT. The normal geomagnetic field (Tn) was calculated using the spherical coefficients recommended by the International Union of Geodesy and Geophysics (IUGG) (model IGRF-2012). As a result of the performed transformations, we obtained a Ta data array which allowed us to construct maps of the abnormal magnetic field (AMF) and perform quantitative interpretation.

Zooplankton sampling and processing

Zooplankton were collected on 9th–20th October 2020 at the 34 stations where CTD sampling was done (Fig. 1) using a closing Juday net with a 180 μm mesh size and a 37 cm mouth opening. At each station, two successive layers were sampled: the layer from the pycnocline to the surface (0 m) and the entire water column from the bottom to the surface. The net was towed vertically with a wire speed of 0.5 m s^{-1}. The volume of the water sampled was calculated from the height of each tow; 100% filtering efficiency was assumed as there were no observed cases of nets clogging. Zooplankton samples were preserved using 10% formalin (4% formaldehyde) for later processing in the laboratory.

In the laboratory, each sample was scanned under a stereomicroscope for large and uncommon species, which were identified to the lowest taxonomic level. All organisms in the samples were enumerated and measured, and the DW of each specimen was predicted from a length-weight regression relationship known for the same species or a morphologically similar organism[38]. Copepods were staged and identified to species; copepods from morphologically indistinguishable genera (i.e. *Pseudocalanus* spp.) were sorted by stage. Meroplankton was grouped to the macrotaxa or to the family level.

Macrozoobenthos sampling and processing

Quantitative samples of macrozoobenthos were collected by a Van Veen grab with an area of 0.12 m^{-2}, with three replicates taken per station. Faunal samples were also obtained from geological grabs and box-corers. All samples were washed through a 0.5 mm mesh and fixed with 4% buffered formalin. Trawling was carried out with an Okkelman sledge enhanced for sampling epibenthos and infauna of the uppermost sediment layer (modification by A.B. Basin and V.A. Spiridonov). If possible, trawling was carried out while drifting; if not, it was carried out at low speed (not exceeding 1–1.5 knots). Depending on the speed, the distance from touch-down to lift-off was between 150 m and 1.5 cables. The coordinates and time of touch-down and lift-off were noted[59]. In total, 41 stations were sampled quantitatively and 51 qualitatively; trawling was carried out at 27 stations. Faunal sample and trawl catch processing was carried out onboard. Provisionary identification of invertebrates to the lowest possible taxonomic level was conducted, dominant groups were assigned, and relative abundance was estimated. Twelve of the quantitative samples, prioritizing areas with hydrological anomalies, were analysed in the laboratory to characterize the fauna of Chaun Bay.

Chlorophyll−a processing

The chlorophyll−a concentrations were determined by the spectrophotometric method. 1.5 L^{-1} water samples were filtered through Vladipore MFAs−Os−3 membrane filters 35 mm in diameter with a 0.8 μm pore size. Subsequently, the filters were dried, dissolved in 5 mL of 90% acetone solution, and refrigerated. One day later, the extract's light absorbance was measured on a Shimadzu PC 3600 spectrophotometer (Japan). The effect of pheophytin on the Chl concentrations was taken into account by acidifying samples with two–three drops of hydrochloric acid solution in acetone, then taking repeated measurements. The Chl concentration in the sample, corrected for the concentrations of pheophytin, was calculated according to[60,61].

Heat budget

Daily 3D fields of temperature, salinity and sea currents, daily 2D fields of sea ice concentration, hourly 2D fields of surface net downward shortwave flux, surface net upward longwave flux, surface upward latent heat flux, surface upward sensible heat flux, were used to calculate the balance of internal energy and heat transport.

The research area for which the heat balance was calculated lies within 167.9°E. - 171.2°E, 68.6°N - 69.82°N and includes Chaun Bay. The study period was from January 1, 2019 to December 31, 2019.

Oceanographic data were taken from oceanographic reanalyses GLORYS12v1[26] and Global Ocean Forecasting System (GOFS) 3.1[27]. Atmospheric data fields were taken from atmospheric reanalysis ECMWF ERA5[28].

The balance of internal heat storage, heat transport and all related parameters were calculated using the following formulas.

The dynamic of average temperature in Chaun Bay was calculated using the formula:

$$\bar{T} = \frac{1}{V}\iiint_V T(x,y,z)dxdydz \tag{6}$$

$V = 84.58 \cdot 10^9 m^3$ - total volume of Chaun Bay
T – sea water temperature (°C)

The dynamic of ice mass in Chaun Bay was calculated using the formula

$$M_{ice} = \iint_S \rho_{ice} \cdot h_{ice} \cdot c_{ice} dx\, dy \tag{7}$$

$\rho_{ice} = 916$ - density of sea ice $\left(\frac{kg}{m^3}\right)$
c_{ice} - Sea ice area fraction
h_{ice} - Sea ice thickness (m)

The dynamic of internal heat storage (J/sec) was calculated using the formula[62]:

$$H_{Storage} = c_p \iiint_V \rho \frac{\partial T}{\partial t} dxdydz \tag{8}$$

$c_p = 4200$ - Heat capacity of water $(\frac{J}{kg \cdot {}^\circ C})$
ρ - Density of water $(\frac{kg}{m^3})$

The changes of internal heat storage were determined by the heat flux at the boundary, which were calculated using the following formulas:

$$F = F_{boundary} + F_{surface} + F_{ice} \quad (9)$$

$F_{boundary}$ - heat flux through vertical open boundary ($\frac{J}{sec}$);
$F_{surface}$ - atmospheric heat flux through surface ($\frac{J}{sec}$);
F_{ice} - heat flux due to ice formation and melting ($\frac{J}{sec}$);
Where:

$$F_{boundary} = c_p \iint_{S_b} \rho \frac{\partial T}{\partial n} v dx dz \quad (10)$$

v – northward sea water velocity;

$$F_{surface} = F_{ssr} + F_{str} + F_{slhf} + F_{sshf} \quad (11)$$

$F_{ssr} = \iint_S Q_{ssr} dxdy$ - surface net downward shortwave flux, integrated over Chaun Bay area

$F_{str} = \iint_S Q_{str} dxdy$ - surface net upward longwave flux, integrated over Chaun Bay area

$F_{slhf} = \iint_S Q_{slhf} dxdy$ - surface upward latent heat flux, integrated over Chaun Bay area

$F_{sshf} = \iint_S Q_{sshf} dxdy$ - surface upward sensible heat flux, integrated over Chaun Bay area

$$F_{ice} = \lambda \iint_S \rho_{ice} \frac{\partial (h_{ice} \cdot c_{ice})}{\partial t} dxdy \quad (12)$$

$\lambda = 333550$- Enthalpy of fusion of sea ice ($\frac{J}{kg}$)

The dynamic of volume-average temperature, dynamic of internal heat storage and all components of heat fluxes were calculated for each day for the period from January 1, 2019 to December 31, 2019. December 31, 2018 was chosen as the starting point (Supplementary Fig. 23). Supplementary Figs. 23–29 show the rates of internal heat storage and all components of heat fluxes for the period from May 15, 2019 to December 15, 2019.

The periods of the most intense changes in internal heat storage happened in summer, when the surface was free from ice. During periods when ice appeared, the rate of change in internal heat storage was small. In 2019, ice began to appear in mid-October. In mid-November, the entire water area of Chaun Bay was covered with ice (Supplementary Fig. 24). The increase of ice thickness continued throughout the cold period of the year, and by the end of March 2020, the ice thickness reached 1.5 meters.

For a simpler understanding of the energy balance of Chaun Bay, the rate of change of internal heat storage and all component fluxes (flux through the surface, flux through the vertical open boundary, heat flux from ice melting processes) were integrated for each month. In this way, the volumes of heat that the water masses of Chaun Bay received (or lost), the volume of heat that passed through the open boundary, the heat flu through the surface and the heat flux that was released or wasted during the ice melting/formation process were obtained. All calculations were made using data from both oceanographic reanalyses. The monthly heat balance for 2019 is shown in Table 1.

Geographical spatial distribution map

Data were interpolated according to the 'Kriging' method; a relative standard error map of the predictions was created by exporting and converting the standard deviation of the 'Kriging' procedure created by Golden Software Surfer 12. Hydrological profiles were made using Ocean Data View (ODV) software. The block scheme was made using Adobe Photoshop CC2019 software. Some maps were corrected manually using linear interpolation.

Data availability

The hydrological, geochemical and hydrochemical data are publicly available at https://doi.org/10.17882/100621. The zoobenthos data available at https://doi.org/10.17882/100246 and zooplankton data available at https://doi.org/10.17882/100278.

Received: 23 June 2023; Accepted: 25 June 2024;
Published online: 22 July 2024

References

1. Filatova, Z. A. Zoogeographic zoning of the northern seas according to the distribution of bivalve mollusks. *Proc. Inst. Oceanol. Acad. Sci. USSR* **23**, 195–215 (1957).
2. Golikov, A. N. et al. in *the series: Studies of the fauna of the seas Ecosystems, flora and fauna of the Chaun Bay of the East Siberian Sea*. Part 1. (St. Petersburg: ZIN RAN, 1994).
3. Helland-Hansen, B. & Nansen, F. The Eastern North Atlantic. The cruises of the "Armauer Hansen", No. 1. *Geofys. Pub1.* **4**, 1–76 (1927).
4. Lozhkin, A. V. & Anderson, P. M. A reconstruction of the climate and vegetation of northeastern Siberia based on lake sediments. *J. Paleontological* **40**, 622–628 (2006).
5. Fukamachi, Y. et al. Direct observations of sea-ice thickness and brine rejection off Sakhalin in the Sea of Okhotsk. *Continental Shelf Res.* **29**, 1541–1548 (2009).
6. *Navigation Book of the East-Siberian Sea*. (Publication of GUNIO MO Russian Federation, St. Petersburg, 1998).
7. Ulyantsev, A. et al. Radioactivity of anthropogenic and natural radionuclides in marine sediments of the Chaun Bay, East Siberian Sea. *Mar. Pollut. Bull.* **195**, 115582 (2023).
8. Moore, W. S. Sources and fluxes of submarine groundwater discharge delineated by radium isotopes. *Biogeochemistry* **66**, 75–93 (2003).
9. Charette, M. A. et al. Salt marsh submarine groundwater discharge as traced by radium isotopes. *Mar. Chem.* **84**, 113–121 (2003).
10. Garcia-Orellana, J. et al. Radium isotopes as submarine groundwater discharge (SGD) tracers: Review and recommendations. *Earth-Sci. Rev.* **220**, 103681 (2021).
11. Charkin, A. N. et al. Discovery and characterization of submarine groundwater discharge in the Siberian Arctic seas: a case study in the Buor-Khaya Gulf, Laptev Sea. *Cryosphere* **11**, 2305–2327 (2017).
12. Diego-Feliu, M. et al. New perspectives on the use of $^{224}Ra/^{228}Ra$ and $^{222}Rn/^{226}Ra$ activity ratios in groundwater studies. *J. Hydrol.* **596**, 126043 (2021).
13. Spall, M. A. Frontogenesis, subduction, and cross–front exchange at upper-ocean fronts. *J. Geophys. Res.* **100**, 2543–2557 (1995).
14. Manucharyan, G. E. & Timmermans, M. L. Generation and separation of mesoscale eddies from surface ocean fronts. *J. Phys. Oceanogr.* **43**, 2545–2562 (2013).
15. Charette, M. A. & Sholkovitz, E. R. Trace element cycling in a subterranean estuary: Part 2. Geochemistry of the pore water. *Geochim. et. Cosmochim. Acta* **70**, 811–826 (2006).
16. Handbook of marine mineral deposits. *CRC Marine Science Series*, 17. (CRC Press: Boca Raton. 2000).
17. Charkin, A. N. et al. The influence of sedimentation regime on natural radionuclide activity concentration in marine sediments of the East Siberian Arctic Shelf. *J. Environ. Radioactivity* **253-254**, 106988 (2022).
18. Kroeger, K. D. et al. Submarine groundwater discharge to Tampa Bay: Nutrient fluxes and biogeochemistry of coastal aquifer. *Mar. Chem.* **104**, 85–97 (2007).
19. Ferronsky, V. & Polyakov V. *Isotopy of the Earth's hydrosphere* (Springer 2012).
20. Bahadori, D. et al. Variations of stable oxygen and hydrogen isotope ratios in the cold and thermal springs of the Bazman volcanic area (in the southeast of Iran). *Environ. Earth Sci.* **78**, 663 (2019).
21. Lowell, R. P. et al. Characteristics of magma-driven hydrothermal systems at oceanic spreading centers. *Geochem., Geophys., Geosyst.* **14**, 1756–1770 (2013).
22. Liu, S.-S. et al. The responses of cyclonic andanticyclonic eddies to typhoon forcing:The vertical temperature-salinitystructure changes

associated with thehorizontal convergence/divergence. *J. Geophys. Res. Oceans* **122**, 4974–4989 (2017).
23. Tontini, F. C. et al. Heat Flow and Near-Seafloor Magnetic Anomalies Highlight Hydrothermal Circulation at Brothers Volcano Caldera, Southern Kermadec Arc, New Zealand. *Geophys. Res. Lett.* **46**, 8252–8260 (2019).
24. Starzhinskii, S. S. & Sormakov, D. A. Deep Electrical Conductivity Anomalies in the Chaun Bay Region Based on Magnetic Variation Sounding Data. *Izv., Phys. Solid Earth* **59**, 765–780 (2023).
25. Aboud, E. et al. The geothermal magmatic system at the northern Rahat volcanic field, Saudi Arabia, revealed from 3D magnetotelluric inversion. *J. Volcanol. Geotherm. Res.* **437**, 107794 (2023).
26. Jean-Michel, L. et al. The Copernicus Global 1/12° Oceanic and Sea Ice GLORYS12 Reanalysis. *Front. Earth Sci.* **9**, 698876 (2021).
27. Cummings, J. A. Operational multivariate ocean data assimilation. *Quart. J. R. Met. Soc., Part C.* **131**, 3583–3604 (2005).
28. Hersbach, H. et al. The ERA5 global reanalysis. *Quart. J. R. Met. Soc.* **146**, 1999–2049 (2020).
29. Gukov A. Y. *Ecology of benthic biocenoses of the Laptev Sea and the East Siberian Sea*. (Doctoral Thesis, Yakutsky University, Yakutsk 2013).
30. Hunt, G. L. et al. The Barents and Chukchi Seas: Comparison of Two Arctic Shelf Ecosystems. *J. Mar. Syst*. 109–110 https://doi.org/10.1016/J.JMARSYS.2012.08.003 (2013).
31. Kim, H.-J. et al. Temporal and spatial variations in particle fluxes on the Chukchi Sea and East Siberian Sea Slopes from 2017 to 2018. *Front. Mar. Sci.* **7**, 609748 (2021).
32. Arrigo, K. R. et al. Primary productivity in the Arctic Ocean: impacts of complex optical properties and subsurface chlorophyll maxima on large-scale estimates. *J. Geophys. Res.* **116**, C11022 (2011).
33. Leopold, P. et al. High Arctic Mytilus spp.: occurrence, distribution and history of dispersal. *Polar Biol.* **42**, 237–244 (2019).
34. Grebmeier, J. M. et al. Ecosystem dynamics of the Pacific-influenced northern Bering and Chukchi Seas in the Amerasian Arctic. *Prog. Oceanogr.* **71**, 331–361 (2006).
35. Gayevskaya, N. S. *Identification key to fauna and flora of the northern seas of the USSR*. ("Sovetskaya Nauka", Moscow, 1948).
36. Mclaughlin, P. A. The Hermit Crabs (Crustacea Decapoda, Paguridea) of Northwestern North America. *Zoologische Verhandelingen* **130**, 1–396 (1974).
37. Smith, S. L. Growth, development and distribution of the euphausiids Thysanoessa raschi (M. Sars) and Thysanoessa inermis (Krøyer) in the southeastern Bering Sea. *Polar Res* **10**, 461–478 (1991).
38. Ershova, E. A. et al. Inter-annual variability of summer mesozooplankton communities of the western Chukchi Sea: 2004–2012. *Polar Biol.* **38**, 1461–1481 (2015).
39. Ershova, E. A. & Kosobokova, K. N. Cross–shelf structure and distribution of mesozooplankton communities in the East-Siberian Sea and the adjacent Arctic Ocean. *Polar Biol.* **42**, 1353–1367 (2019).
40. Moore, S. E. et al. Bowhead Whales along the Chukotka Coast in Autumn. *Arctic* **48**, 155–160 (1995).
41. Moore, W. S. Fifteen years experience in measuring Ra-224 and Ra-223 by delayed coincidence counting. *Mar. Chem.* **109**, 188–197 (2008).
42. Moore, W. S. & Arnold, R. Measurement of ^{224}Ra and ^{223}Ra in coastal waters using delayed coincidence counter. *J. Geophys. Res.* **101**, 1321–1329 (1996).
43. Garcia-Solsona, E. et al. Uncertainties associated with ^{224}Ra and ^{223}Ra measurements in water via a Delayed Coincidence Counter (RaDeCC). *Mar. Chem.* **109**, 198–219 (2008).
44. Moore, W. S. & de Oliveira, J. Determination of residence time and mixing processes of the Ubatuba, Brazil, inner shelf waters using natural Ra isotopes. *Estuar. Coast. Shelf Sci.* **76**, 512–521 (2008).
45. Moore, W. S. & Cai, P. Calibration of RaDeCC systems for ^{224}Ra and ^{223}Ra measurements. *Mar. Chem.* **156**, 130–137 (2013).
46. Hougham, A. L. & Moran, S. B. Water mass ages of coastal ponds estimated using ^{223}Ra and ^{224}Ra as tracers. *Mar. Chem.* **105**, 194–207 (2007).
47. Burnett, W. C. et al. Radon and radium isotopes as tracers of submarine groundwater discharge – results from the Ubatuba Brazil SGD assessment intercomparison. *Estuar. Coast. Shelf S.* **76**, 501–511 (2008).
48. Dulaiova, H. et al. Assessment of groundwater discharge into West Neck Bay, New York, via natural tracers. *Cont. Shelf. Res.* **26**, 1971–1983 (2006).
49. Moore, W. S. Ages of continental shelf waters determined from ^{223}Ra and ^{224}Ra. *J. Geophys. Res. -Oceans* **105**, 117–222 (2000).
50. Grasshoff, K. et al. *Methods of Seawater Analysis*. 2nd Edition. (Verlag Chemie: Weinheim, Germany, 1983).
51. Pavlova, G. et al. Intercalibration of Bruevich's method to determine the total alkalinity in seawater. *Oceanology* **48**, 438–443 (2008).
52. Tishchenko et al. The measurement of pH values in seawater using a cell without a liquid junction. *Oceanology* **41**, 813–822 (2001).
53. *Guide to Best Practices for Ocean CO_2 Measurements*. (eds. et al.) http://cdiac.ornl.gov/oceans/Handbook_2007.html (PICES, Special Publication 3, 2007).
54. Lewis, E. & Wallace, D. W. R. *Program developed for CO_2 System Calculations. ORNL/CDIAC-105*. (Carbon Dioxide Information Analysis Center, Oak Ridge National Laboratory, Oak Ridge, Tenn. 1998).
55. Mehrbach, C. et al. Measurement of the apparent dissociation constants of carbonic acid in seawater at atmospheric pressure. *Limnol. Oceanogr.* **18**, 897–907 (1973).
56. Dickson, A. G. & Millero, F. J. A comparison of the equilibrium constants for the dissociation of carbonic acid in seawater media. *Deep-Sea Res* **34**, 1733–1743 (1987).
57. Dickson, A. G. Standard potential of the reaction: AgCl(s) + 1/2H2(g) = Ag(s) + HCl(aq), and the standard acidity constant of the ion HSO4 in synthetic sea water from 273.15 to 318.15. *K. J. Chem. Thermodyn.* **22**, 113–127 (1990).
58. Mucci, A. The solubility of calcite and aragonite in seawater at various salinities, temperatures, and one atmosphere total pressure. *Am. J. Sci.* **283**, 780–799 (1983).
59. Chernova, N. V. et al. Marine fish of the Chaunskaya Bay— A shallow estuary of the East-Siberian Arctic. *Reg. Stud. Mar. Sci.* **52**, 102344 (2022).
60. Jeffrey, S. W. & Humphrey, G. F. New spectrophotometric equations for determining chlorophyll *a, b,* c_1 and c_2 in higher plants, algae and natural phytoplankton. *Biochem. Physiol. Pflanz.* **167**, 191–194 (1975).
61. Lorenzen, C. J. Determination of Chlorophyll and Pheopigments: Spectrophotometric Equations. *Limnol. Oceanogr.* **12**, 343–346 (1967).
62. Jackson, R. H. & Straneo, F. Heat, Salt, and Freshwater Budgets for a Glacial Fjord in Greenland. *J. Phys. Oceanogr.* **46**, 2735–2768 (2016).
63. Nikulina, E. A. Einhornia a new genus for electrids formerly classified as the Electra crustulenta species group (Bryozoa, Cheilostomata). *Schriften des. Naturwissenschaftlichen Ver. f. ür. Schleswig-Holst.* **69**, 29–40 (2007).
64. Lubinsky, I. Studies on Mytilus edulis L. of the "Calanus" expeditions to Hudson Bay and Ungava Bay. *Can. J. Zool.* **36**, 867–881 (1958).
65. Koehn, R. K. et al. Genetic differentiation of Mytilus edulis in eastern North America. *Mar. Biol.* **79**, 117–126 (1984).
66. Feder, H. M. et al. A review of apparent 20th century changes in the presence of mussels (Mytilus trossulus) and macroalgae in Arctic Alaska, and of historical and paleontological evidence used to relate mollusc distributions to climate change. *Arctic* **56**, 391–407 (2003).
67. Sukhotin, A. A. et al. Growth and longevity of Mytilus edulis (L.) from northeast Europe. *Mar. Biol. Res.* **3**, 155–167 (2007).
68. Gwiazda, R. et al. Freshwater seepage into sediments of the shelf, shelf edge, and continental slope of the Canadian Beaufort Sea. *Geochem., Geophys., Geosyst.* **19**, 3039–3055 (2018).

Acknowledgements
This work was supported by the state assignments no. AAAA-A20-120011090005-7 and no. FMWE–2024-0021. The zooplankton data analyses were supported by the Russian Science Foundation grant no. 23-17-00121. We acknowledge the use of imagery from the NASA Worldview application (https://worldview.earthdata.nasa.gov), part of the NASA Earth Observing System Data and Information System (EOSDIS).

Author contributions
A.N.C. conceived the original idea and supervised this work, data analysis, manuscript composition, figure preparation, designed the towed robotic system "Smart Fish", manuscript editing. K.N.K. biological (zooplankton) data analysis, manuscript composition, figure preparation, manuscript editing. E.A.E. biological data analysis, manuscript composition, figure preparation, manuscript editing V.L.S. biological data analysis, manuscript composition, figure preparation. G.D.K. biological data analysis, manuscript composition, figure preparation. P.Y.S. chemical data analysis, manuscript composition, figure preparation. A.E.L. isotope data analysis, manuscript composition, figure preparation. O.V.D. geological data analysis, manuscript composition. T.A.G. oceanographic data analysis, manuscript composition, figure preparation, designed the towed robotic system "Smart Fish". E.I.Y. geological data analysis, manuscript composition, figure preparation. A.M.S. designed the towed robotic system "Smart Fish". P.A.F. heat budget. V.A.K. isotope data analysis, figure preparation. S.A.Z. geomagnetic data analysis, manuscript composition, figure preparation. E.A.B. geomagnetic data analysis, manuscript composition, figure preparation. A.S.U. geological data analysis. E.V.E. determination of trace elements by plasma-mass spectrometry. D.A.Y. biological data analysis. K.A.K. biological data analysis. O.L.Z. biological data analysis. A.V.G. biological data analysis. P.P.T. biological data analysis. A.A.D. 3D model distributions of hydrological parameters.

Competing interests
The authors declare no competing interests.

Additional information
Supplementary information The online version contains supplementary material available at https://doi.org/10.1038/s43247-024-01529-x.

Correspondence and requests for materials should be addressed to Alexander N. Charkin.

Peer review information *Communications Earth & Environment* thanks the anonymous reviewers for their contribution to the peer review of this work. Primary Handling Editors: Heike Langenberg. A peer review file is available.